5-2023

Archival Search for X-ray Emission From Type Ib/c Supernovae

Michael Dixon
Trinity University, michaelwdixon6280@gmail.com

Archival Search for X-ray Emission From Type Ib/c Supernovae

by

Michael Dixon

An honors thesis submitted to the Department of Physics & Astronomy at

TRINITY UNIVERSITY

in partial fulfillment of the requirements for the
Bachelor of Science in Physics
May 2024

Accepted by .....
Prof. Kelvin Cheng

Accepted by .....
Prof. Nirav Mehta

Accepted by .....
Prof. David Pooley

Accepted by .....
Prof. Orrin Shindell

Accepted by .....
Prof. Jennifer Steele, Chair

Accepted by .....
Prof. Niescja Turner

Accepted by .....
Prof. Dennis Ugolini

Archival Search for X-ray Emission From Type Ib/c Supernovae

by

Michael Dixon

Submitted to the Department of Physics & Astronomy
on 2023-April-10, in partial fulfillment of the
requirements for the Bachelor of Science in Physics

Abstract

We present results from an ongoing archival search for X-ray emission from all known Type Ib/c supernovae using data from the Chandra X-ray Observatory. For each supernova, we search all possible observations to find those with coverage in X-rays. For those observations with coverage of a supernova, we extract an X-ray spectrum at the location of the supernova and create response files. We model those spectra with an absorbed hot plasma model in order to determine luminosities or set upper limits. These results are then used to determine or set limits on the mass-loss history of the pre-supernova stars, thus giving insight into the late stages of stellar evolution.

Thesis Supervisor: Prof. David Pooley

Acknowledgments

Words cannot express my gratitude to the tireless efforts of Dr. David Pooley in supporting my research and preventing anything from standing in my way, including myself. I could not have undertaken this journey without him and the faculty of the Trinity University Physics & Astronomy Department, to whom I am greatly indebted. Additionally, this project would not have been possible without the generous funding of the Murchison Foundation.

I am further grateful to Dr. Nirav Mehta, who sparked my original interest in research at Trinity University. Lastly, to Erin Burns, Elizabeth Coughlin, Madison Reich, and all the members of Dr. Pooley's research team: I am truly thankful for your moral support. My time on this team has genuinely been improved by your group's presence.

Contents

Chapter 1

Introduction

Type I supernovae (SN) are produced by the stellar core collapse of supergiant stars and are defined by a lack of H emission lines within their spectra (Fig. 1-1) [1]. There are three primary variants of Type I SN: Type Ia, Type Ib, and Type Ic. My research focuses almost entirely on Type Ib/c SN which are evolutionarily distinguished from Type Ia SN in that they are formed by single massive stars core collapsing rather than the explosion of a white dwarf star that has approached the Chandrasekhar limit [1]. Type Ib/c SN are further observationally distinguished from Type Ia SN by the lack of a singularly ionized Si emission line within their spectra [2]. Type Ic SN are additionally distinguished from Type Ib SN due to their lack of He emission lines. Given the size of the stars (typically larger than 20 $M_{\odot}$) which collapse to form Type Ib/c SN, the lack of detected H in these SN is quite surprising. One possible explanation for this phenomenon is that H is lost over the course of these stars' lifetimes due to stellar winds blowing the H away. If this is the case, that H would become part of the circumstellar medium (CSM) surrounding these stars. When Type Ib/c SN occur, they produce ejecta which interacts with the CSM to produce shock waves that radiate X-ray light. Thus, further investigation of the X-rays produced by these shocks seems prudent to determine the mass-loss history of the pre-SN stars.

1.1 Late Stage Stellar Evolution

The massive stars which collapse to form Type Ib/c SN are known to have strong stellar winds their entire lives. However, only the mass lost immediately before the SN explosion is relevant to the early interactions of SN ejecta and CSM [3]. As such, we focus on the late stage of these stars' stellar evolution, starting with their time as red supergiants.

Red supergiants are defined by having masses at least 8 solar masses ($M_{\odot}$) large and luminosities in the range of tens or even hundreds of thousands of solar luminosities ($L_{\odot}$) [4]. They are considered quite cool with temperatures typically lower than 4100 K and have massive radii of several hundred to even a thousand times that of the Sun ($R_{\odot}$). These large radii mean that the gravitational force

Figure 1-1: Type Ib supernova SN 2008D shown in X-ray light on the left and visible light on the right with corresponding image positions. Credit: NASA/Swift Science Team/Stefan Immler

at the surface of these supergiants is quite weak compared to that of other stars. Thus, stellar winds are able to easily carry off mass from the surface of these stars.

Typical wind speeds for red supergiants are within the range of $10 - 50$ km s^{-1} which correlate to mass-loss rates of $10^{-6} - 10^{-5} M_{\odot}$ yr^{-1} [3]. A number of red supergiants have been known to undergo a brief super-wind phase which correlate to mass-loss rates on the order of $10^{-4} - 10^{-3} M_{\odot}$ yr^{-1}. These stars, however, are relatively uncommon. Assuming mass-loss rates stay relatively constant leading up to the SN explosion, the circumstellar density can be given by

$$\rho_{cs} = \frac{\dot{M}}{4\pi u_w r^2} \tag{1}$$

where $\dot{M}$ is the mass-loss rate of the star in kg s^{-1}, u_w is the velocity of solar wind in m s^{-1}, and r is radial distance from the star in m. This equation and many of the following derivations are based upon the assumption of spherical geometry of CSM, ejecta, and shock waves. There is, however, evidence that the shape of the ejecta and CSM may be more complex, a topic which will only be briefly touched upon within this thesis.

Red supergiants larger than 20 $M_{\odot}$ go on to become Wolf-Rayet [WR] stars [5]. Type Ib/c SN are created primarily from stars of this size or larger. WR stars exhibit strong solar winds with equally strong mass-loss. For WR stars, $u_w \approx 1000$ km s^{-1} [6]. The defining characteristic of WR stars is that these stars have already burned through or otherwise lost all of their H and now burn He within their cores. This stage of stellar evolution is relatively short lived (less than 10 million years), yet how long stars remain in this stage determines whether they are progenitors to Type Ib or Type Ic SN. This time frame is dependant upon the initial mass of the star. For the purposes

of this paper, Type Ib and Type Ic SN are too similar to differentiate. In fact, Type Ib and Ic SN are so similar they are often referred to as Type Ibc SN with no differentiation [7].

Once WR stars burn through the He and other heavy elements within their core, the star core collapses [2]. This core-collapse is followed by the collapse of the outer star layers into the core. These outer star layers are then ejected outwards in all directions from the star as super-heated material known as "ejecta." This is known as the SN event. The interactions of the ejecta with the CSM then create shock waves [3][6][8].

1.2 Shock Waves

Shock waves occur when perturbations within a gas, liquid, or plasma are propagated through the material faster than the speed of sound within the material [9]. As the disturbance is travelling faster than the speed of sound, it cannot behave like a sound wave, and change between the regions before and ahead of the shock wave is discontinuous (Fig. 1-2). Thus, shock waves occur when one material crashes into another stationary material faster than the speed of sound. There are three conservation laws which dictate shock wave properties, known as shock conditions. These are

$$\rho_1 v_1 = \rho_2 v_2, \tag{2}$$

$$\rho_1 v_1 \left(\frac{1}{2}v_1^2 + w_1\right) = \rho_2 v_2 \left(\frac{1}{2}v_2^2 + w_2\right), \tag{3}$$

and

$$p_1 + \rho_1 v_1^2 = p_2 + \rho_2 v_2^2 \tag{4}$$

where ρ is mass density, v is velocity, p is pressure, w is enthalpy per unit mass, and subscripts 1 and 2 refer to the material in the regions ahead of and behind the shock respectively. For simplicity, we assume a perfect gas where $w = \gamma pV/(\gamma - 1)$ where γ is the ratio of the specific heat capacities and V is the specific volume. The assumption of a perfect gas gives a fourth condition

$$\frac{p_1 V_1}{T_1} = \frac{p_2 V_2}{T_2} \tag{5}$$

where T is temperature. We additionally define $U = v_1 - v_2$ where U is the speed of the shock wave.

We may next rearrange Eq. 2, 3, 4, and 5 into the following ratios

$$\frac{p_2}{p_1} = \frac{2\gamma M_1^2 - (\gamma - 1)}{(\gamma + 1)}, \tag{6}$$

$$\frac{\rho_2}{\rho_1} = \frac{v_1}{v_2} = \frac{(\gamma + 1)}{(\gamma - 1) + 2/M_1^2}, \tag{7}$$

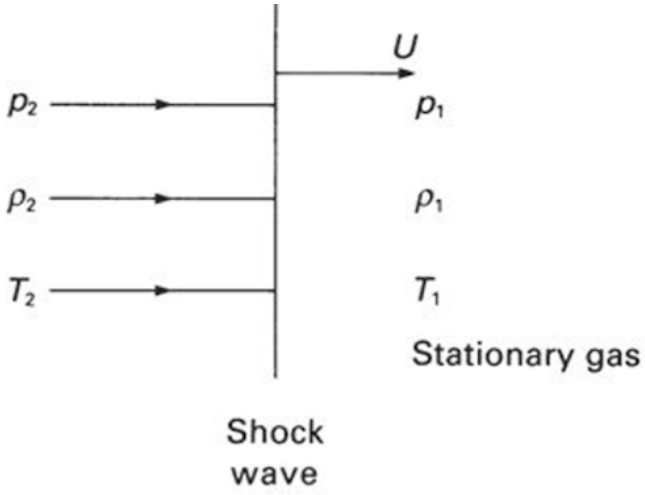

Figure 1-2: A shock wave propagating through a stationary gas at velocity U. Credit: High Energy Astrophysics 3e, M.S. Longair

and

$$\frac{T_2}{T_1} = \frac{[2\gamma M_1^2 - (\gamma - 1)][2 + (\gamma - 1)M_1^2]}{(\gamma + 1)^2 M_1^2} \tag{8}$$

where $M_1 = U/(\gamma p_1/\rho_1)^{1/2}$ is the Mach Number, the ratio of the shock wave velocity over the velocity of sound within the unperturbed gas. Within the limit of very strong shocks ($M_1 >> 1$) we may simplify Eq. 6, 7, and 8 to

$$\frac{p_2}{p_1} = \frac{2\gamma M_1^2}{(\gamma + 1)}, \tag{9}$$

$$\frac{\rho_2}{\rho_1} = \frac{v_1}{v_2} = \frac{(\gamma + 1)}{(\gamma - 1)}, \tag{10}$$

and

$$\frac{T_2}{T_1} = \frac{2\gamma(\gamma - 1)M_1^2}{(\gamma + 1)^2}. \tag{11}$$

We next consider the more complex case of the supersonic piston (Fig. 1-3). In this scenario, a piston moves down a cylinder full of gas at supersonic speed U. The velocity of the shock wave v_s is yet unknown, but we can say that from the perspective of the shock front, $|v_s| = v_1$ where v_1 is now the velocity of the "stationary" gas moving into the shock wave front. This allows us to solve for v_1, a known term. Thus, solving Eq. 7 for v_1 and inserting our definitions of U and v_s, we may say

$$v_s = \frac{(\gamma + 1)}{4} U + \sqrt{\frac{\gamma p_1}{\rho_1} + \frac{(\gamma + 1)^2 U^2}{16}}. \tag{12}$$

In the limit of strong shocks ($U >> \gamma p_1/\rho_1$), this reduces down to

$$v_s = \frac{(\gamma + 1)U}{2}. \tag{13}$$

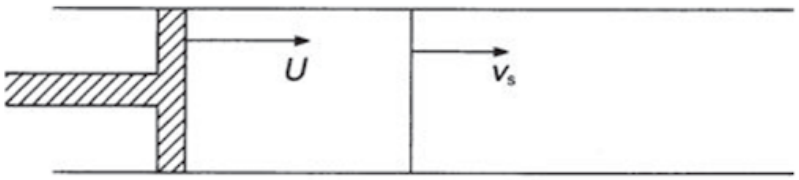

Figure 1-3: A piston propagating through a stationary gas at velocity U. Credit: High Energy Astrophysics 3e, M.S. Longair

Lastly, we note that SN shocks fall into a category of shock waves known as radiative shocks. Radiative shocks are defined by having a "radiative relaxation layer" (rrl) following the shock [10]. The rrl is large compared to that of the shock front due to the number of particle collisions necessary for the material to cool. Since the rrl only affects the radiative cooling of the material, Eq. 2 and 4 stay the same for the rrl, becoming

$$\rho_1 v_1 = \rho_2 v_2 = \rho_3 v_3, \tag{14}$$

and

$$p_1 + \rho_1 v_1^2 = p_2 + \rho_2 v_2^2 = p_3 + \rho_3 v_3^2 \tag{15}$$

where the subscript 3 denotes the area within the rrl. The rrl has a lower temperature and velocity than the post shock region accompanied by an increase in particle density and pressure. This increase in density can be quite large. In fact, the defining characteristic of a radiative shock is that the ratio ρ_3/ρ_1 can be arbitrarily large in the presence of a strong shock whereas the limit of ρ_2/ρ_1 in a non-radiative shock is approximately 4. This large ratio of mass densities is necessary for the formation of SN shocks.

1.3 SN Shock Waves

Several days after the initial SN explosions the ejecta travelling outwards from the explosion center is moving at a constant velocity [3]. The density of this ejecta can be expressed with

$$\rho_{ej} = \rho_0 \left(\frac{t}{t_0}\right)^{-3} \left(\frac{v_0 t}{r}\right)^n \tag{16}$$

where n is the constant for the power law expression. Physical arguments imply that $\rho_{ej} \propto r^{-1}$ in the inner ejecta and that $n > 5$ in the outer ejecta [11]. For general WR progenitor stars $n \approx 10.2$ due to their radiative envelope [12][3]. However, modelling of Type Ib/c SN has revealed a value of $n = 10$ to be more accurate [6].

From the perspective of the CSM, this ejecta travelling outwards acts as the supersonic piston driving the shock wave forward [3]. From the perspective of the ejecta, the CSM acts as the piston

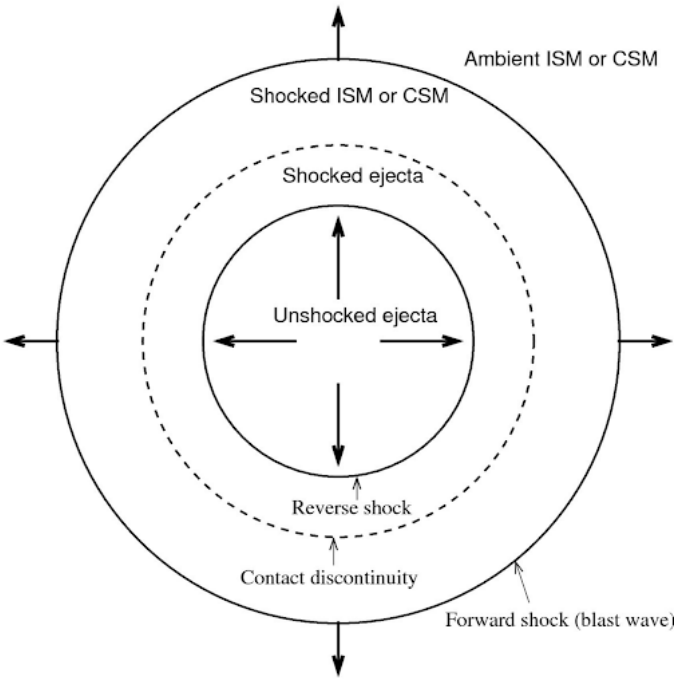

Figure 1-4: SN shock diagram. Credit: Dynamical Evolution and Radiative Processes of Supernova Remnants, Stephen P. Reynolds

driving a reverse shock backwards. This reverse shock travels inwards in mass, but since the ejecta is moving outwards the shock still travels outwards in physical space. This creates four primary regions in space: the unshocked CSM, the shocked CSM, the shocked ejecta, and the unshocked ejecta (Fig. 1-4). The unshocked and shocked CSM are divided by the forward shock, the unshocked and shocked ejecta are divided by the reverse shock, and the shocked CSM and shocked ejecta are divided by a contact discontinuity.

For the purposes of the derivations that follow, we assume the combination of the shocked CSM and shocked ejecta to be a thin shell. Solutions derived from this thin shell approximation differ by $\sim 30\%$ from more accurate solutions which take the size and shape of the shocked gas into account [13]. Using Eq. 1 and 16, the momentum equation for this shocked thin shell is

$$M_s \frac{dv_s}{dt} = 4\pi R_s^2[\rho_{ej}(v_{ej} - v_s)^2 - \rho_{cs} v_s^2] \tag{17}$$

where M_s, R_s, and v_s are the mass, radius, and velocity of the shocked thin shell. We additionally define $M_s = M_{cs} + M_{rev}$ where M_{cs} is the mass of the shocked CSM and M_{rev} is the mass of the shocked ejecta, $M_{cs} = \dot{M} R_s / u_w$, and $M_{rev} = 4\pi \int_{R_s}^{\infty} \rho(r) r^2 dr$. Using the assumption of free expansion of ejecta whereby $v_s = R_s/t$, we may insert these definitions into Eq. 17 and solve to obtain

$$R_s(t) = \left[\frac{8\pi \rho_0 t_0^3 v_0^n u_w}{(n-4)(n-3)\dot{M}}\right]^{1/(n-2)} t^{(n-3)(n-2)}. \tag{18}$$

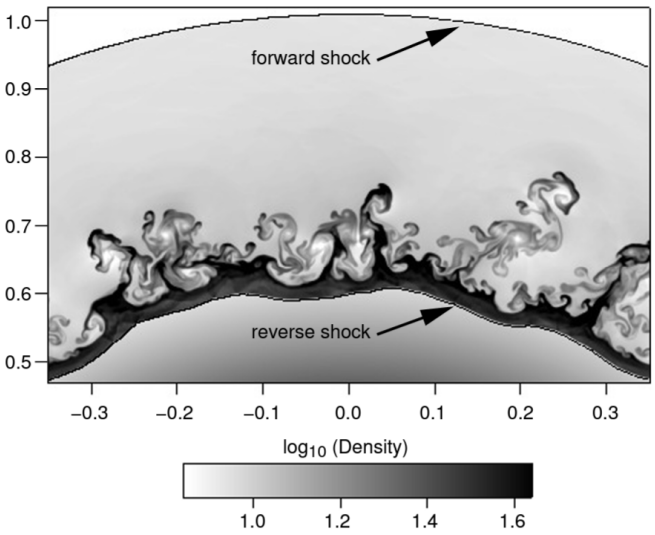

Figure 1-5: Two dimensional calculation of Rayleigh-Taylor instability in an $n = 6$ SN using piecewise parabolic method hydrodynamic code. Credit: Thermal and non-thermal emission from circumstellar interaction, Roger A. Chevalier and Claes Fransson

By taking the derivative with respect to time of Eq. 18, we say the velocity of the forward shock is given by

$$v_s(t) = \frac{n-3}{n-2} v_{ej} \tag{19}$$

while the velocity of the reverse shock is given by

$$v_{rev} = \frac{v_{ej}}{(n-2)} \tag{20}$$

since $v_{rev} = v_s - v_{ej}$. For Type Ib/c SN, $v_s \approx 0.1c$ [6]. Lastly, we say the density of the shocked ejecta is given as

$$\rho_{rev} = \frac{(n-4)(n-3)}{2} \rho_{csm}. \tag{21}$$

For a more detailed derivation of Eq. 21 see [3].

The actual structure of these SN shocks are more complex. Due to the fact that the shocked CSM has lower density than the shocked ejecta and is decelerating the shocked ejecta, a Rayleigh-Taylor instability forms at the contact discontinuity between the two (Fig. 1-5). For a full analysis of the shape of this discontinuity, see [14]. However, since the Rayleigh-Taylor instability does not distort general dynamics of the shock structure, evolution, or luminosity, we will not discuss it further here.

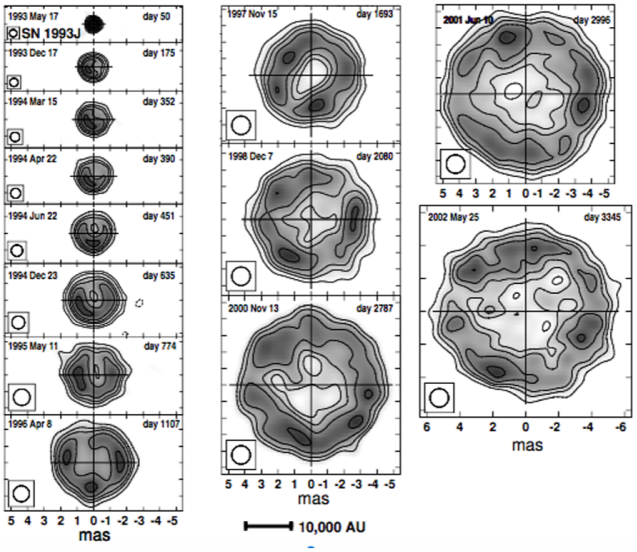

Figure 1-6: Thermal emissions of SN 1993J between 50 to 3335 days after explosion. As this is a Type II SN, the emissions are in radio waves, but the expansion process looks much the same in the X-ray range for Type Ib/c SN. Credit: Thermal and non-thermal emission from circumstellar interaction, Roger A. Chevalier and Claes Fransson

1.4 SN X-Ray Emission

The temperatures of the shocked CSM and shocked ejecta can be given by the following equations

$$T_{cs} = 1.36 \times 10^9 \left(\frac{n-3}{n-2}\right)^2 \left(\frac{v_{ej}}{10^4 \text{ km s}^{-1}}\right) \text{K} \tag{22}$$

and

$$T_{rev} = \frac{T_c s}{(n-3)^2} \tag{23}$$

[3]. These shocked materials give off thermal bremsstrahlung radiation on the order of 10^7 K (Fig. 1-6). However, for Type Ib/c SN, additional non-thermal mechanisms are required to explain magnitude of X-ray luminosity produced [6]. Two good candidates for this are inverse Compton and synchrotron emission. Close to the time the initial SN event, inverse Compton scattering is believed to play a significant role in producing X-ray emissions while late time emission are believed to be influenced more by synchrotron emission. Thus, despite the temperature of the shocked CSM being higher than the shocked ejecta, since the density of the shocked ejecta is several orders of magnitude larger than that of the shocked CSM we are able to approximate the entire luminosity of the shock wave as that given off by the shocked ejecta [3].

The shocked ejecta luminosity is given by

$$L_{rev} = 4\pi R_s^2 \frac{1}{2} \rho_{rev} v_{rev}^3. \tag{23}$$

This can be simplified using Eq. 18, 20, and 21 to give

$$L_{ej} = \frac{(n-3)(n-4)}{4(n-2)^3} \frac{\dot{M} v_s^3}{u_w}. \tag{24}$$

The general formula for the relation between the energy flux of an object and its luminosity is given by

$$L = 4\pi r^2 f \tag{25}$$

where r is distance to the object and f is energy flux. Plugging Eq. 25 and our values of $u_w = 1000$ km s^{-1}, $v_s = 0.1c$, and $n = 10$ into Eq. 24 and solving for $\dot{M}$ gives

$$\dot{M} = 2.3 \times 10^{-18} r^2 f \text{ g s}^{-1} \tag{26}$$

where $\dot{M}$ is the mass-loss rate of pre-Type Ib/c SN WR stars. This equation is quite simplistic, ignoring variations in u_w, v_s, and n between different progenitor stars and SN and requiring the use of a thin shell approximation of shocked materials post-SN. This equation is, however, a useful baseline estimate for determining pre-SN WR mass-loss rates as it is a direct relation between the mass-loss rate of the pre-SN progenitor star and energy flux measurements taken post-SN. Given that the distance to SN host galaxies is generally known, we now have the information necessary to create basic mass-loss histories of pre-SN progenitor WR stars for Type Ib/c SN based upon measurements of energy flux.

Chapter 2

Data Reduction and Analysis

We analyzed 61 serendipitous observations in the X-ray range of six different SN taken by the Chandra X-ray Observatory. Of these observations, only 45 gave viable data used in our final analysis (Tab. A.1). We analyzed twenty-five observations of SN 1983I, ten observations of SN 1983N, one observation of SN 1990U, three observations of SN 1991N, four observations of SN 1999ec, and two observations of SN 2003gk. SN 2003gk is classified as a Type Ib SN, but there is disagreement as to the correct classification of the other five SN. SN 1983I, SN 1990U, and SN 1991N are classified as either a Type Ib or Ic SN. SN 1983N is classified as either a Type Ia or Ib SN. SN 1999ec is classified as either a Type Ia, Ib, or Ic SN.

2.1 DS9

For each photon that it detects, Chandra records arrival time, arrival position, and energy. We receive this data in the form of ".fits" file types. We then load each ".fits" file for each observation into the program SAOImageDS9 (hereafter DS9). DS9 is astronomical data visualization software which converts the data of photon positions and energies into an image. Once the image has been created, we classify the observation as "Supernova Detected" (Fig. 2-1), "Supernova Not Detected" (Fig. 2-2), or "Supernova Off-Screen" (Fig. 2-3).

Since the images created by DS9 are in the X-ray range, the appearance of the images can be quite different than that of their optical light counterparts. A side-by-side comparison of the two images reveal almost no similarities between the two. As such, when we detect SN in the X-ray range, we find no usable data in counterpart images in the optical range.

"Supernova Off-Screen" cases are observations in which the location of the SN being observed was partially or completely outside of the field of view of Chandra at the time the observation was recorded. We attempted to avoid these cases by choosing only Chandra observations within a few arcminutes of known SN, however, some such observations resulted in SN on the edge of Chandra's field of view. As such, for these cases no further data analysis was conducted and the observations

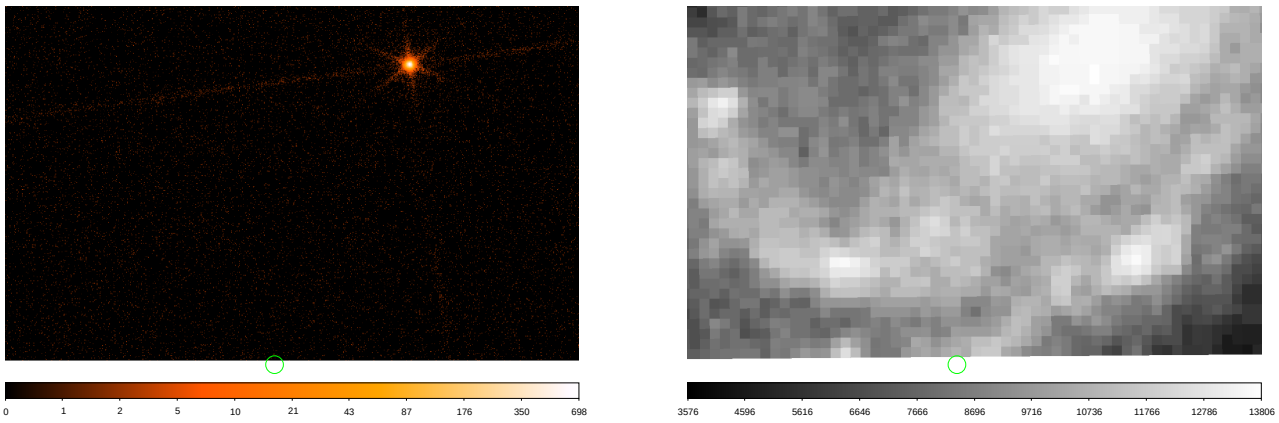

Figure 2-1: *Left*: Chandra X-ray image of ObsID 3144 of SN 1983N off-screen shown in green circle of 1.5 arcsecond radius. Shown in logarithmic scale. Image size of 1.5×1 arcminutes. *Right*: Optical light counterpart shown in linear scale.

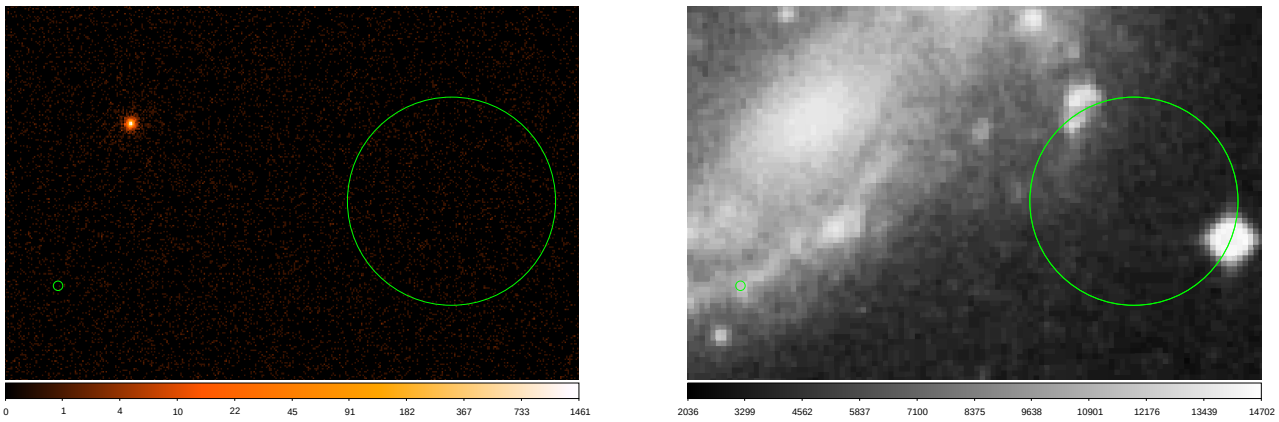

Figure 2-2: *Left*: Chandra X-ray image of ObsID 10782 of SN 1983N on-screen but undetected shown in green circle of 1.5 arcsecond radius. Larger green circle defines background region. Shown in logarithmic scale. Image size of 3×2 arcminutes. *Right*: Optical light counterpart shown in linear scale.

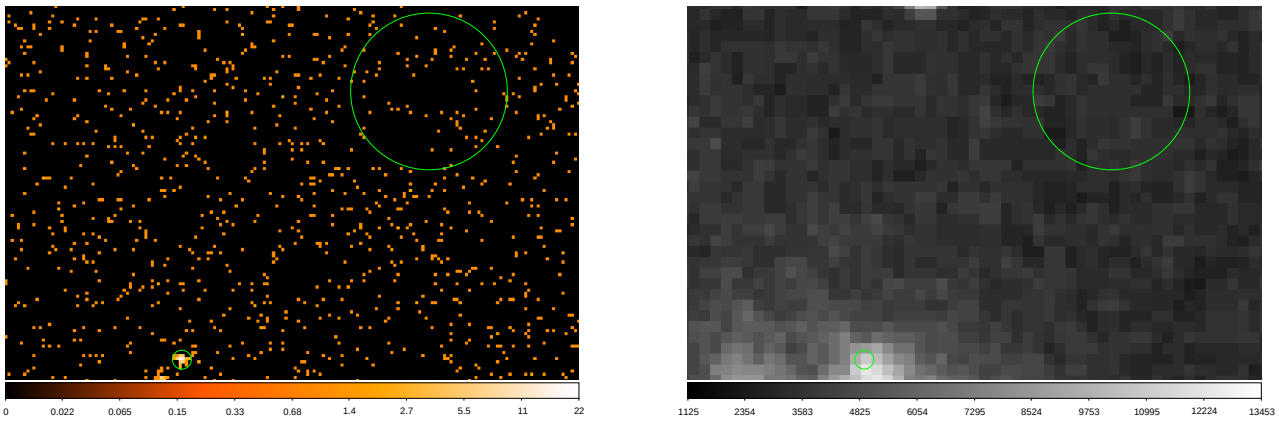

Figure 2-3: *Left*: Chandra X-ray image of ObsID 21004 of SN 2003gk on-screen and detected shown in green circle of 1.5 arcsecond radius. Larger green circle defines background region. Shown in logarithmic scale. Image size of 1.5×1 arcminutes. *Right*: Optical light counterpart shown in linear scale.

were not used within our final results. These account for 16 of our 61 observations. "Supernova Not Detected" cases are defined as observations where the location of the SN being observed was within the field of view of Chandra at the time the observation was recorded, but for which the only X-rays detected were those which were consistent with background radiation. These account for 43 of our observations. Lastly, "Supernova Detected" cases are defined as observations where the location of the SN being observed was within the field of view of Chandra at the time the observation was recorded, and for which X-rays detected at the location of the SN were greater in number and magnitude than that which would be consistent with background radiation. These account for the two observations of SN 2003gk.

For observations we classify as "Supernova Detected" or "Supernova Not Detected," we set the energy scale within DS9 to logarithmic and create two circular regions on the image. The first is the source region which we center around the SN location. The size of this region is 1.5 arcseconds in radius which is just large enough to encompass the SN being observed without including extra background. The next region is the background region which we center around a point on the image where no radiation other than background radiation is detected. The background region is typically 15-20 arcseconds in radius, depending upon how much space with only background radiation present is available. We then save these regions as ".reg" files. These files define which portion of photon counts are within the selected regions of the DS9 image.

2.2 Specextract

We then run the program Specextract using the ".fits" and ".reg" files for our data. Specextract is a script supplied by the Chandra X-ray Center which runs a sequence of tools to create spectra for Chandra observations. The ".fits" file contains information on the photons detected during

each observation. The ".reg" files contains information on the specific locations of our source and background regions. Specextract filters the ".fits" matrix to only include the data points contained within the ".reg" file. From there, Specextract filters out any "bad pixels" of unusable data.

Next, Specextract determines the location of the center of the source ".reg" file. This is not necessarily the physical center of the region defined by the ".reg" file, but rather the highest energy point on the detector within the given region. At this point, Specextract has the information needed to create a response matrix file (RMF). RMFs contain information about energy redistribution. Energy redistribution refers to the fact that the energy levels recorded by Chandra for each photon that made contact with the detector may be different than the actual energy of the photon. This is primarily due to two factors: imperfect charge collection which lowers the recorded energy peak and detector effects such as Fano-like and electronic noise which broaden the recorded energy peak of the photon. RMFs contain, for each photon, the probability of being recorded at each possible energy channel. Specextract creates an RMF for both the source and background region of each given observation.

Next, Specextract creates an ancillary response file (ARF) for both the source and background region. The ARF contains the effective area of the region of the detector contained within the ".reg" file. The effective area is a multiplicative product of the physical area of the detector which is measured in cm^2, the quantum effeciency of the detector, and the relative ability of the mirrors to focus X-ray photons of various energies. The quantum effeciency of the detector is the probability of the detector to convert a single incident photon into an observed detector count. As the quantum effeciency is unitless, the effective area is measured in cm^2.

Finally, Specextract creates spectra for both the source and background regions of the SN. These spectra contain the number of photon counts as a function of detector channel within each given region. This final product is saved as a ".pi" file along with the corresponding RMFs and ARFs. At this point, the data is now ready to be fit and modeled.

2.3 Background Analysis

We then load our ".pi" files into the Sherpa package. Sherpa was developed by the Chandra X-ray Center for the purpose of fitting and modeling X-ray data. The raw spectra created by Specextract has a range of about 0 to 14.5 keV. We first filter this data to the range of 0.4 to 8 keV. Anything above or below this range contains too much noise to be relevant to model. Additionally, the X-ray source peaks we expect the find are well within this range. We then begin the process of fitting a model to the spectra of the background region.

We use Sherpa's variation of the Levenberg-Marquardt algorithm to fit the background spectra [15]. We choose this algorithm primarily because the background spectra is relatively simple and predictable. As such, we are able to consistently choose well-fitting initial parameter values. This allows us to utilize the Levenberg-Marquardt algorithm for its speed despite the algorithm's failure

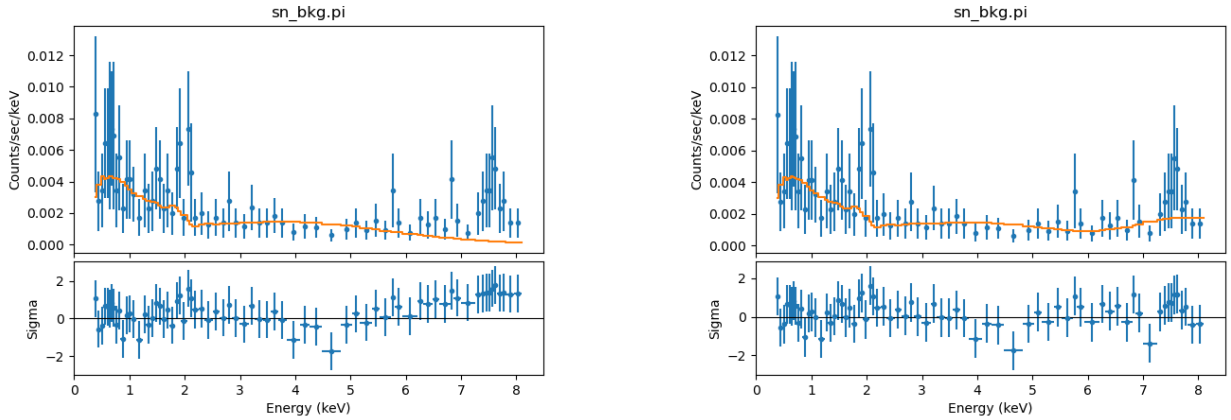

Figure 2-4: *Left*: Top graph is an additive dual power law multiplied by dual absorption models fit to the background of ObsID 16024 of SN 1983N. Bottom graph is the residuals. Fit does not match data in the upper energy range. *Right*: Same observation of SN 1983. Background model fit has been given an additional additive Gaussian component. The model now better fits the data in the upper energy range.

to model complex cases with unknown ideal initial parameter values. As we are using a Levenberg-Marquardt algorithm, we set the model to evaluate fit statistics as a chi-squared model with Gehrels weighting [16]. We choose this statistic for two reasons. First, the Levenberg-Marquaradt algorithm works best with chi-squared statistics, and second, the Gehrels weighting is designed for low count data, such as our background spectra.

We first attempt to fit the background using two additive power law models each multiplied by an absorption model. Our absorption models calculate the cross section for interstellar medium (ISM) absorption of X-rays via a sum of gas-phase, grain-phase, and molecule ISM absorption. The only free variable within this model is hydrogen column density. Our power law models are simple photon power laws defined by

$$A(E) = KE^{-\alpha} \tag{27}$$

where α is the dimensionless photon index of the power law and K is the photons/keV/cm^2/s at 1 keV. Each of these are their own free variable. For our initial fit attempt, we set $\alpha_1 = 0$ and $\alpha_2 = 2$.

We then fit our models to the background spectra, check the reduced statistic, and check a residual plot of our fit against the background spectra. While any reduced statistic less than 1 is considered to be an acceptable fit, we checked the residuals to look for any sections where our model did not intersect the error bars for multiple data points in a row (Fig. 2-4). For such cases with an incorrectly fitted section of data, we froze both power law components of our model and began to revise our model. In every case, we found the addition of a Gaussian function to be all that was necessary to properly fit our model to the background spectra. Once we corrected our background models, we froze all components of the background model and began fitting our source spectra.

2.4 Source Analysis: Upper Limits

For observations where no SN were detected, we calculated upper limits of energy flux from the source spectra. Our models (described below) are based upon the most appropriate physical models for SN X-ray emission. We change both our fitting algorithm and fitting statistic for the source spectrum fitting. For our fitting algorithm, we use the Nelder-Mead Simplex algorithm [17]. The Nelder-Mead Simplex algorithm is robust and converges to global minimum in complex model cases such as our source spectra. Additionally, the Nelder-Mead Simplex algorithm is a non-derivative method with no gradiant information, which makes it ideal for fitting models with correlated parameters. For our fitting statistic, we use the cstat maximum likelihood statistic for Poisson data [18]. This fitting statistic is necessary as our source spectra often have zero to only a handful of counts. Additionally, we set the elemental abundances according to those defined by [19] except for elements not listed which are given zero abundance.

We fit our source spectra with an absorption component multiplied by the Astrophysical Plasma Emission Code (APEC) spectrum [20]. Unlike our background model fit, we freeze the hydrogen column density value within the absorption model to the value defined by NASA's nH tool at the location of each SN observation. The values listed by the nH tool are derived from [21], [22], and [23]. APEC contains four free variables: the temperature of the plasma, the metal abundance of the plasma, the redshift of the plasma, and the normalization of the model. The metal abundance of the plasma include the abundances of He, C, N, O, Ne, Mg, Al, Si, S, Ar, Ca, Fe, and Ni, and is frozen at solar abundance. The redshift of the plasma is frozen at zero.

At this point, we make two calculations of possible energy flux upper limit values. The first is with plasma temperature set to 1 keV, and the second is with plasma temperature set to 10 keV; these are typical values for well-detected SNe. For each value, we freeze the plasma temperature and run the fit to find the highest normalization that is consistent with zero detected counts. We then check our confidence intervals of our normalization value. We then freeze the APEC normalization value to the best fit and upper bound normalization values output by the confidence interval added together. At this point, SHERPA has all the information needed to calculate the energy flux using the APEC model. We record each of our two final values, one for the 1 keV case and one for the 10 keV case for each observation.

2.5 Source Analysis: Detections

For the two observations where the SN was detected, we kept the same elemental abundances, fitting algorithm, and fitting statistic as we used for the SN not detected cases. We additionally fit our source spectra with the same absorption model with the hydrogen column density frozen in the same manner as the previous SN not detected cases. We multiply this absorption model by the Variable Astrophysical Plasma Emission Code (VAPEC) spectrum. VAPEC is different from

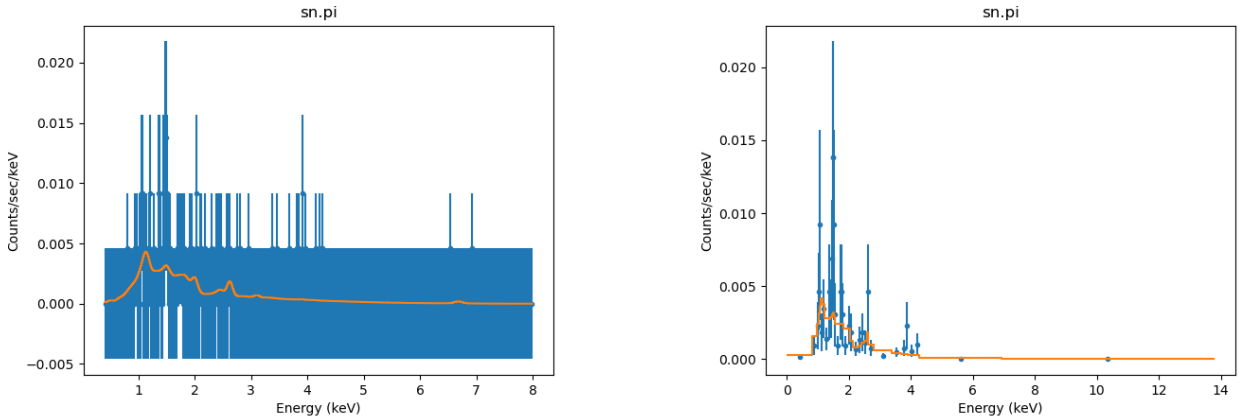

Figure 2-5: *Left*: Plot of VAPEC multiplied by absorption model fit to spectra of ObsID 21004 of SN 2003gk. Error bars are calculated with a chi squared model and are not those used for the purpose of fitting. *Right*: Same plot of fit and spectra with photon counts grouped to two per detector for the purpose of clarity.

APEC in that each of the metal abundances of the plasma (He, C, N, O, Ne, Mg, Al, Si, S, Ar, Ca, Fe, and Ni) are their own free variables. Once again, redshift is set to zero. We additionally freeze the metal abundance of He to solar abundance.

We then fit our model to the source spectra and check confidence intervals of each free variable. For metal abundances whose range is unconstrained by the fit, we freeze their value to that of solar abundance and then fit our model again. For ObsID 21004, Mg, Al, and Ca were all found to be unconstrained during the first fitting attempt and were subsequently frozen. For the second fitting attempt, C, N, and Ne were found to also be unconstrained and were then frozen as well. The third fitting attempt resulted in no unconstrained variables (Fig. 2-5). For ObsID 22271, Mg and Al were found to be unconstrained during the first fitting attempt and frozen. In the second fitting attempt, C, N, and Ne were found to be unconstrained and frozen. In the third fitting attempt, O was found the be unconstrained and frozen. The fourth fitting attempt resulted in no unconstrained variabled (Fig. 2-6)

We then take a sample of 10,000 fluxes of the unabsorbed model for each observation. We then take the mean, median, and standard deviation of these fluxes. Finally, we plot a probability distribution of the sample of fluxes.

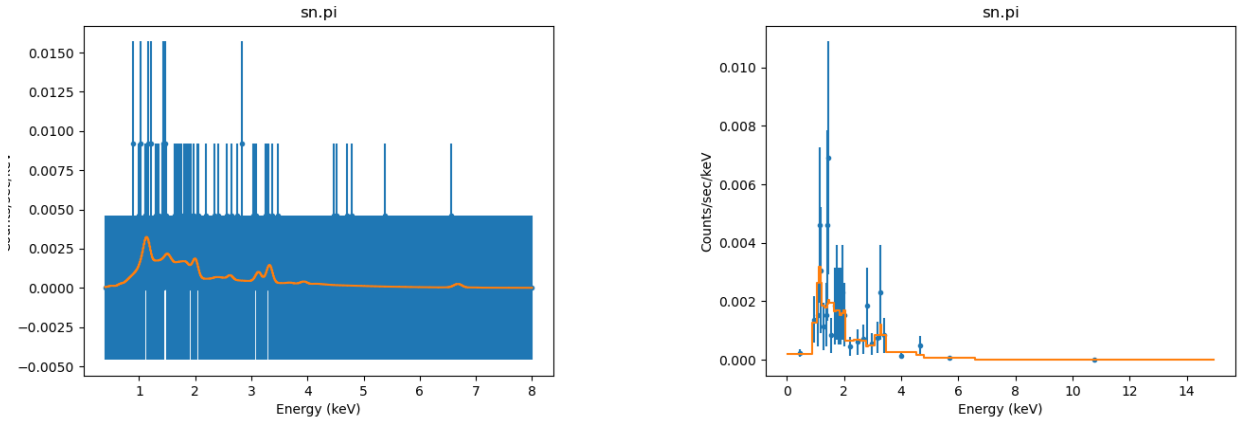

Figure 2-6: *Left*: Plot of VAPEC multiplied by absorption model fit to spectra of ObsID 22271 of SN 2003gk. Error bars are calculated with a chi squared model and are not those used for the purpose of fitting. *Right*: Same plot of fit and spectra with photon counts grouped to two per detector for the purpose of clarity.

Chapter 3

Results

3.1 Upper Limit Results

Table 3.1 displays the upper limit energy fluxes calculated for each SN observation. In order to calculate the corresponding mass-loss upper limits using Eq. 26, the median value of the calculated distances to the SN host galaxies listed within the NASA/IPAC Extragalactic Database was used. Table 3.2 displays these results. Given that calculated mass-loss upper limits are within the order of 10^{-7} $M_{\odot}$/year, we believe it is unlikely that the shock waves from these SN were passing through H at $0.1c$ (the assumption of the mass-loss rate calculation) at the time that these observations were recorded. It is possible that interaction was taking place, but with a much slower shock velocity than was assumed.

Table 3.1: Energy Flux Upper Limits

SN	Observation Id	1 keV [10^{-15} erg/cm^2/s/keV]	10 keV [10^{-15} erg/cm^2/s/keV]
1983I			
	859	1.27	2.72
	2148	0.04	0.09
	4160	3.42	12.38
	10403	1.01	1.29
	10404	1.48	1.86
	10775	1.24	1.58
	10776	7.85	0.91
	10777	1.01	1.25
	10778	1.13	1.49
	10779	1.18	1.49
	10780	1.05	1.36
	10781	1.17	1.71
	10782	1.59	2.02
	10801	1.91	6.09
	10824	2.95	3.67
	17102	0.39	0.36
	17103	6.32	8.06
	17104	3.73	2.66
	17105	1.51	1.27
	18768	4.31	3.83
	18769	0.60	1.48
	18785	0.67	0.61
	18786	0.64	0.63
	18787	1.70	1.50
	18823	2.27	2.04
1983N			
	793	1.00	2.55
	2064	1.82	4.03
	12992	0.11	0.46
	12993	1.60	3.85
	12994	0.92	2.24
	12996	0.35	2.01
	13241	0.08	0.17
	14332	0.48	0.99
	14342	0.62	1.58
	16024	0.17	0.28
1990U			
	11230	0.09	0.20
1991N			
	2939	7.94	18.05
	16025	9.91	19.69
	19891	6.96	11.80
1999ec			
	11228	1.14	2.44
	14799	3.74	7.18
	14914	1.41	2.76
	14915	1.69	3.17

Observation Identifiers are given to each observation to indicate target, proposal, and observation configuration.

Table 3.2: Mass-Loss Upper Limits

SN	Observation Id	1 keV [10^{-7} $M_\odot$/year]	10 keV [10^{-7} $M_\odot$/year]
1983I			
	859	0.69	1.48
	2148	0.02	0.05
	4160	1.86	6.74
	10403	0.55	0.70
	10404	0.81	1.01
	10775	0.68	0.86
	10776	4.27	0.50
	10777	0.55	0.68
	10778	0.62	0.81
	10779	0.64	0.81
	10780	0.57	0.74
	10781	0.64	0.93
	10782	0.87	1.10
	10801	1.04	3.31
	10824	1.61	2.00
	17102	0.21	0.20
	17103	3.44	4.38
	17104	2.03	1.45
	17105	0.82	0.69
	18768	2.34	2.08
	18769	0.32	0.81
	18785	0.36	0.33
	18786	0.35	0.34
	18787	0.93	0.81
	18823	1.24	1.11
1983N			
	793	0.08	0.28
	2064	0.15	0.33
	12992	0.01	0.04
	12993	0.13	0.31
	12994	0.08	0.18
	12996	0.03	0.16
	13241	0.01	0.01
	14332	0.04	0.08
	14342	0.05	0.13
	16024	0.01	0.02
1990U			
	11230	0.21	0.43
1991N			
	2939	3.51	7.97
	16025	4.37	8.69
	19891	3.07	5.21
1999ec			
	11228	1.11	2.38
	14799	3.64	6.99
	14914	1.37	2.68
	14915	1.65	3.09

Observation Identifiers are given to each observation to indicate target, proposal, and observation configuration.

3.2 Detected Source Results

Table 3.3 displays the mean, median, and standard deviation energy fluxes calculated for the two SN 2003gk observations. Distance to SN 2003gk was calculated the same way as the other SN. Table 3.4 displays our final mass-loss history results. Mass-loss rates on the order of 10^{-5} $M_{\odot}$/year are to be expected and thus our results are within the proper order of magnitude [3][24][25]. Additionally, the probability distribution functions of both our observations reveal no abnormalities within our fit models (Figs. 3-1 & 3-2).

Our results indicate that the shocks from SN 2003gk were passing through H shed by the pre-SN WR progenitor star at the time these observations were detected. These preliminary results appear to support the idea that pre-SN WR stars shed at least a portion of their H prior to exploding as Type Ib/c SN. While the order of magnitude of our mass-loss results are promising, the exact values may not be accurate for three primary reasons.

1. **Our SN spectra fit models are too simplistic.** The VAPEC model used to fit both observations of SN 2003gk assumes a constant temperature throughout the shocked SN ejecta. In reality, however, the shocked SN ejecta likely has a range of temperatures at different points.

2. **We assume average pre-SN wind speeds and SN shock speeds.** In reality, every Type Ib/c SN will have different wind and shock velocities. As such, it would be better to find a best fit model with $\dot{M}$, u_w, and v_s as separate free variables.

3. **We neglect the effects of inverse Compton scattering and synchrotron emission.** There is evidence to suggest that both of these types of X-ray emission may play a role in Type Ib/c SN emissions [6]. Our calculation assumes complete thermal bremsstrahlung radiation. In order to determine inverse Compton scattering and synchrotron emission effects, if any, our SN observations would need to be for longer periods of time with more data points available.

As such, we limit our conclusion to the following. At some point in its life, the pre-SN WR progenitor star for SN 2003gk shed at least a portion of its H to the CSM. This may indicate a larger pattern among other Type Ib/c SN progenitors, but more data is needed.

Table 3.3: SN 2003gk Energy Flux Measurements [10^{-14} erg/cm^2/s/keV]

Observation Id	Mean	Median	Standard Deviation
21004	7.02	6.86	1.89
22271	5.54	5.43	1.48

Table 3.4: SN 2003gk Mass-Loss Rates [10^{-5} $M_{\odot}$/year]

Observation Id	Mean	Median	Standard Deviation
21004	3.36	3.29	0.91
22271	2.66	2.60	0.71

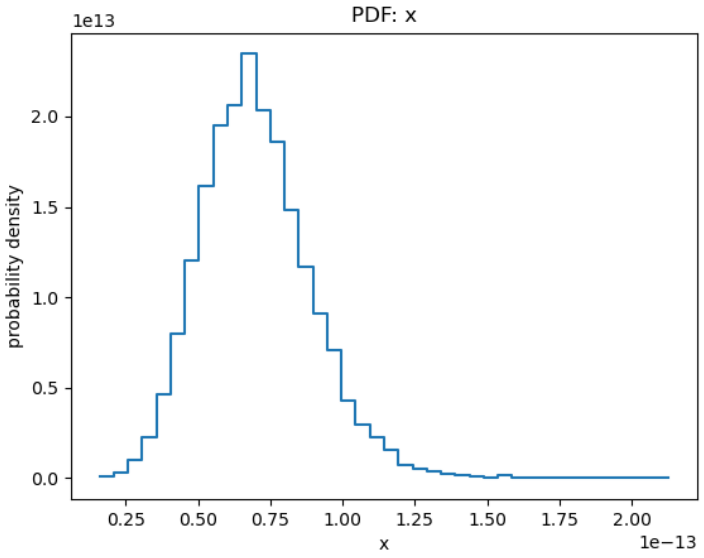

Figure 3-1: Probability distribution function of a sample of 10,000 fluxes from ObsID 21004 of SN 2003gk

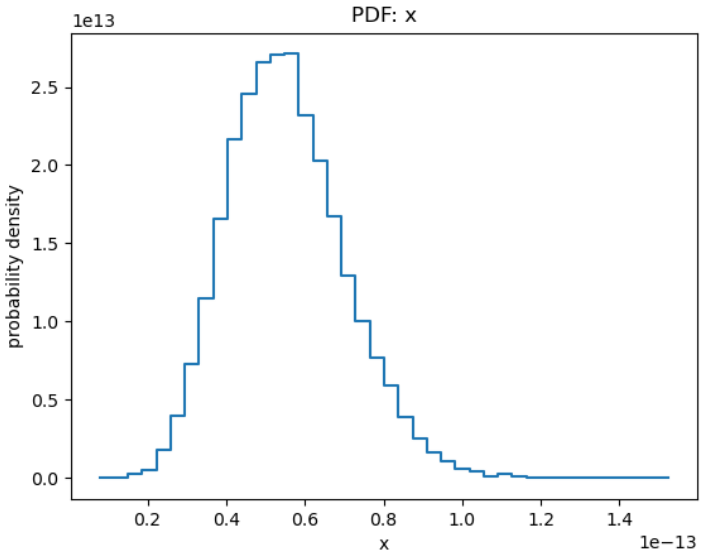

Figure 3-2: Probability distribution function of a sample of 10,000 fluxes from ObsID 22271 of SN 2003gk

Chapter 4

Future Work

The future direction of my research consists of three primary objectives.

1. **We must continue to search for X-ray bright Type Ib/c SN.** This involves combing through Chandra observations taken near the location of known Type Ib/c SN to determine the existence of serendipitous observations of SN. This process was briefly touched upon in the DS9 section of this paper. Chandra observations made within a few arcminutes of known SN are examined to determine whether they include the location of said SN within their images. Those that do are recorded and those that do not are discarded.
2. **We must automate the simple stages of the data reduction and analysis process.** Once possible serendipitous SN observations are identified, many of the stages of their analysis are repetitive and do not require human input. The vast majority of the time that I analyzed the data for this research project was spent entering Sherpa and DS9 commands that were identical for each observation. Human input is only required to ensure that spectra fits are accurate after first attempts have been made. Reduction in analysis time is necessary due to the scale of this project. To give a sense of the magnitude of the endeavor, from 2018 alone, there are 529 observations to examine. This paper, the culmination of a year and a half of my research, was only able to analyze 61.
3. **We must build up more SN Type Ib/c X-ray statistics.** The results obtained from my research present a baseline from which to built up a larger body of data surrounding Type Ib/c SN. However, with only two detected observations of SN analyzed, it is hard to draw any firm conclusions about the mass-loss history of these SN. Ideally with more data points from more SN, we could draw specific conclusions about when and how H is lost from SN progenitor stars in the time leading up to their explosion.

Appendix A

Tables

The following is a list of all SN observations analyzed in my research. Observations where the SN were off-screen are excluded.

Table A.1: Chandra X-Ray SN Observations (On-Screen)

SN	Observation Id	Date & Time	Exposure Time [s]	Stellar Location [deg]
1983I				
	859	D:2000-03-25 T:06:08:25	82528	180:46:33.193, +44:31:56.933
	2148	D:2001-02-06 T:06:24:59	52259	180:47:09.765, +44:32:26.801
	4160	D:2003-07-23 T:00:34:15	96628	180:47:26.222, +44:31:36.470
	10403	D:2008-11-09 T:20:17:35	39357	180:47:31.252, +44:32:09.459
	10404	D:2008-11-12 T:16:45:46	21288	180:47:28.818, +44:32:09.908
	10775	D:2008-11-08 T:14:15:18	32864	180:47:31.287, +44:32:09.472
	10776	D:2008-11-11 T:22:50:34	27013	180:47:28.809, +44:32:09.872
	10777	D:2008-11-06 T:15:06:22	29744	180:47:31.313, +44:32:09.489
	10778	D:2008-11-11 T:00:19:46	35910	180:47:28.716, +44:32:09.936
	10779	D:2008-11-20 T:07:22:39	29897	180:47:26.919, +44:32:10.099
	10780	D:2008-11-25 T:09:51:46	28113	180:47:25.053, +44:32:10.203
	10781	D:2008-11-26 T:21:04:24	25852	180:47:25.136, +44:32:10.242
	10782	D:2008-11-29 T:11:32:38	25110	180:47:25.155, +44:32:10.163
	10801	D:2008-11-13 T:14:24:31	27997	180:47:28.786, +44:32:09.949
	10824	D:2008-11-30 T:04:20:59	11061	180:47:25.215, +44:32:10.354
	17102	D:2016-02-26 T:19:06:50	116034	180:47:13.726, +44:31:46.526
	17103	D:2016-03-01 T:00:15:27	64918	180:47:13.673, +44:31:46.537
	17104	D:2016-02-16 T:09:07:55	61972	180:47:14.121, +44:31:48.028
	17105	D:2016-02-18 T:13:41:19	117691	180:47:14.574, +44:31:47.570
	18768	D:2016-02-11 T:03:56:40	94660	180:47:14.086, +44:31:48.083
	18769	D:2016-02-21 T:13:14:42	73877	180:47:14.607, +44:31:47.587
	18785	D:2016-02-28 T:15:44:02	69010	180:47:13.697, +44:31:46.492
	18786	D:2016-03-02 T:07:49:22	68828	180:47:13.717, +44:31:46.503
	18787	D:2016-04-14 T:06:50:30	28063	180:47:26.289, +44:31:43.353
	18823	D:2016-04-15 T:09:20:07	24340	180:47:26.091, +44:31:43.316

SN	Observation Id	Date & Time	Exposure Time [s]	Stellar Location [deg]
1983N				
	793	D:2000-04-29 T:13:54:43	53984	204:16:53.530, -29:53:23.155
	2064	D:2001-09-04 T:23:58:38	11822	204:13:33.525, -29:53:43.240
	12992	D:2011-09-04 T:06:06:28	68558	204:13:55.267, -29:53:45.799
	12993	D:2011-03-15 T:12:02:00	52352	204:17:00.395, -29:50:21.535
	12994	D:2011-03-23 T:03:42:51	154002	204:17:03.487, -29:50:24.203
	12996	D:2011-03-29 T:15:58:18	55050	204:17:21.319, -29:50:43.180
	13241	D:2011-03-18 T:21:35:44	81321	204:17:00.430, -29:50:21.520
	14332	D:2011-08-29 T:18:29:09	55379	204:13:55.266, -29:53:45.783
	14342	D:2011-12-28 T:09:50:58	70292	204:15:34.756, -29:49:54.000
	16024	D:2014-06-07 T:08:26:15	31995	204:15:03.415, -29:52:35.939
1990U				
	11230	D:2009-08-11 T:00:08:25	27478	346:13:26.008, +12:18:23.521
1991N				
	2939	D:2003-01-25 T:00:20:59	49360	159:40:58.455, +53:30:41.766
	16025	D:2014-06-11 T:04:19:24	11046	159:41:42.746, +53:30:04.812
	19891	D:2016-10-22 T:16:14:25	37737	159:41:08.418, +53:30:25.211
1999ec				
	11228	D:2010-07-18 T:11:05:39	14493	94:03:44.280, -21:22:10.309
	14799	D:2013-04-07 T:21:50:23	12636	94:04:43.743, -21:22:40.430
	14914	D:2012-12-30 T:04:23:51	21857	94:05:38.865, -21:22:13.371
	14915	D:2013-08-24 T:04:21:38	21527	94:05:20.036, -21:22:20.146
2003gk				
	21004	D:2018-08-21 T:01:53:29	17848	345:25:21.173, +2:16:08.103
	22271	D:2019-08-05 T:15:27:20	17518	345:25:27.139, +2:16:07.728

Bibliography

[1]L. A. L. da Silva, "The classification of supernovae", Astrophysics and Space Science **202**, 215–236 (1993).

[2]A. V. Filippenko, "Supernovae and their massive star progenitors", in The fate of the most massive stars, Vol. 332, edited by R. Humphreys and K. Stanek, Astronomical Society of the Pacific Conference Series (Sept. 2005), p. 34.

[3]R. A. Chevalier and C. Fransson, "Thermal and non-thermal emission from circumstellar interaction", in *Handbook of supernovae*, edited by A. W. Alsabti and P. Murdin (Springer International Publishing, Cham, 2017), pp. 875–937.

[4]E. M. Levesque, P. Massey, K. A. G. Olsen, B. Plez, E. Josselin, A. Maeder, and G. Meynet, "The effective temperature scale of galactic red supergiants: Cool, but not as cool as we thought", The Astrophysical Journal **628**, 973–985 (2005).

[5]A. Heger, C. L. Fryer, S. E. Woosley, N. Langer, and D. H. Hartmann, "How massive single stars end their life", The Astrophysical Journal **591**, 288–300 (2003).

[6]R. A. Chevalier and C. Fransson, "Circumstellar emission from type Ib and Ic supernovae", The Astrophysical Journal **651**, 381 (2006).

[7]A. J. Williams, "Initial statistics from the Perth Automated Supernova Search", Publications of the Astronomical Society of Australia **14**, 208–13 (1997).

[8]Nymark, T. K., Fransson, C., and Kozma, C., "X-ray emission from radiative shocks in type II supernovae", Astronomy and Astrophysics **449**, 171–192 (2006).

[9]M. S. Longair, "Aspects of plasma physics and magnetohydrodynamics", in *High energy astrophysics*, 3rd ed. (Cambridge University Press, 2011) Chap. 11, pp. 314–319.

[10]D. Weinberg, "Shocks", in *Lecture notes in radiative gas dynamics, Ohio State University*, URL: https://www.astronomy.ohio-state.edu/weinberg.21/A825/notes7.pdf (2007), pp. 37–45.

[11]R. A. Chevalier and N. Soker, "Asymmetric envelope expansion of supernova 1987A", The Astrophysical Journal **341**, 867 (1989).

[12]A. Sakurai, "On the problem of a shock wave arriving at the edge of a gas", Communications on Pure and Applied Mathematics **13**, 353–370 (1960).

[13]R. A. Chevalier, "Self-similar solutions for the interaction of stellar ejecta with an external medium.", The Astrophysical Journal **258**, 790–797 (1982).

[14]R. A. Chevalier, J. M. Blondin, and R. T. Emmering, "Hydrodynamic instabilities in supernova remnants: Self-similar driven waves", The Astrophysical Journal **392**, 118 (1992).

[15]J. J. Moré, "The Levenberg-Marquardt algorithm: Implementation and theory", in *Lecture notes in mathematics, Berlin Springer Verlag*, Vol. 630 (1978), pp. 105–116.

[16]N. Gehrels, "Confidence limits for small numbers of events in astrophysical data", The Astrophysical Journal **303**, 336 (1986).

[17]J. C. Lagarias, J. A. Reeds, M. H. Wright, and P. E. Wright, "Convergence properties of the Nelder–Mead simplex method in low dimensions", SIAM Journal on Optimization **9**, 112–147 (1998).

[18]W. Cash, "Parameter estimation in astronomy through application of the likelihood ratio", The Astrophysical Journal **228**, 939–947 (1979).

[19]J. Wilms, A. Allen, and R. McCray, "On the absorption of X-rays in the interstellar medium", The Astrophysical Journal **542**, 914–924 (2000).

[20]R. K. Smith, N. S. Brickhouse, D. A. Liedahl, and J. C. Raymond, "Collisional plasma models with APEC/APED: Emission-line diagnostics of hydrogen-like and helium-like ions", The Astrophysical Journal **556**, L91–L95 (2001).

[21]HI4PI Collaboration: Ben Bekhti, N., Flöer, L., Keller, R., Kerp, J., Lenz, D., Winkel, B., Bailin, J., Calabretta, M. R., Dedes, L., Ford, H. A., Gibson, B. K., Haud, U., Janowiecki, S., Kalberla, P. M. W., Lockman, F. J., McClure-Griffiths, N. M., Murphy, T., Nakanishi, H., Pisano, D. J., and Staveley-Smith, L., "HI4PI: A full-sky survey based on EBHIS and GASS", Astronomy and Astrophysics **594**, A116 (2016).

[22]Kalberla, P. M. W., Burton, W. B., Hartmann, Dap, Arnal, E. M., Bajaja, E., Morras, R., and Pöppel, W. G. L., "The Leiden/Argentine/Bonn (LAB) survey of galactic HI - Final data release of the combined LDS and IAR surveys with improved stray-radiation corrections", Astronomy and Astrophysics **440**, 775–782 (2005).

[23]J. M. Dickey and F. J. Lockman, "H I in the galaxy.", Annual Review of Astronomy and Astrophysics **28**, 215–261 (1990).

[24]V. V. Dwarkadas, "Massive star mass-loss revealed by X-ray observations of young supernovae", Proceedings of the International Astronomical Union **14**, 83–87 (2018).

[25]L. M. Dray, C. A. Tout, A. I. Karakas, and J. C. Lattanzio, "Chemical enrichment by Wolf—Rayet and asymptotic giant branch stars", Monthly Notices of the Royal Astronomical Society **338**, 973–989 (2003).